Journal of Power Sources 516 (2021) 230701

Contents lists available at ScienceDirect

Journal of Power Sources

journal homepage: www.elsevier.com/locate/jpowsour

In-situ exfoliation and integration of vertically aligned graphene for high-frequency response on-chip microsupercapacitors

Iman Khakpour [a], Amin Rabiei Baboukani [a], Shahrzad Forouzanfar [b], Anis Allagui [a,c], Chunlei Wang [a,*]

[a] Department of Mechanical and Materials Engineering, Florida International University, Miami, FL33174, USA
[b] Department of Electrical and Computer Engineering, Florida International University, Miami, FL33174, USA
[c] Department of Sustainable and Renewable Energy Engineering, University of Sharjah, Sharjah, United Arab Emirates

HIGHLIGHTS

- Bipolar electrochemistry is used to deposit vertically aligned graphene nanosheets.
- Fabricated microsupercapacitors showed very high electrochemical capacitance.
- The device exhibited close-to-ideal capacitive behavior even at high frequencies.

ARTICLE INFO

Keywords:
Bipolar electrochemistry
Vertically aligned graphene
On-chip microsupercapacitor
High-frequency filter

ABSTRACT

Fast response on-chip micro-supercapacitors (MSCs) with large energy storage capabilities are highly in demand for high-frequency circuits and systems such as alternating current (AC) line filters. Devices with vertically aligned graphene thin-film electrodes were shown to be promising in maintaining close-to-ideal capacitive behavior at high frequencies due to low ionic and electric resistances. This study investigates a novel in-situ integration of vertically aligned graphene layers with micro-sized gold current collectors in which a modified bipolar electrochemistry method has been applied. The electrochemical analysis revealed a high average capacitance of 640 μF cm^{-2} ($C.V^{-1}cm^{-2}$) at a scan rate of 2 mV s^{-1} for the fabricated MSCs and their excellent stability even after 50000 successive charge-discharge cycles by constant current. Most notably, the electrochemical impedance spectroscopy results revealed that the MSCs exhibited very fast response and close-to-ideal capacitive behavior even at around 1000 Hz. Specifically, the phase angle and specific capacitance measured at 120 Hz were −81.2 deg and 65.2 μF cm^{-2}, respectively, in addition to a cut-off frequency of 3486 Hz at which the impedance angle is −45 deg. The device was tested as the capacitive energy storage component in a standard AC line filter, and its performance was found comparable to a commercial off-the-shelf aluminum electrolytic capacitor.

1. Introduction

Given the recent developments in the fabrication of microelectronic devices, embedded micro-sized energy storage systems in which they can be directly integrated with other microelectronic compounds are becoming more and more in demand [1–3]. Microsupercapacitors (MSCs) are considered as promising alternatives to bulky electrolytic capacitors or batteries for on-chip applications given their simplicity in design, long lifetime, low heating effects, and safety considerations [4–10]. In addition, MSCs —as two-terminal devices— can be connected in parallel and series to meet the required capacity, voltage, and current of the intended load [11]. Supercapacitors can be categorized into three groups of (1) electrical double-layer capacitors (EDLCs), (2) pseudocapacitors, and (3) hybrid capacitors, based on the charge storage mechanisms [12–14], and as such, their specifications and applications vary accordingly [10,14]. The EDLCs store the electrical charge in the double-layer structure formed at the electrolyte/electrode interface and exhibit a much faster response than the other two types [11–13,15]. However, the frequency response of EDLCs, which is typically in the range of several hundred milliseconds to several seconds, is still lagging

* Corresponding author.
E-mail address: wangc@fiu.edu (C. Wang).

https://doi.org/10.1016/j.jpowsour.2021.230701
Received 22 August 2021; Received in revised form 8 October 2021; Accepted 25 October 2021
Available online 30 October 2021

behind that of conventional aluminum electrolytic capacitors (AEC), which generally is in the range of several milliseconds. When applied to MSCs, even though the short diffusion paths between the microelectrodes lower their time constants, the mechanistic weakness still limits their high-frequency on-chip applications, which necessitates exploring alternative strategies to further enhance the frequency response of MSCs.

Among all the different available and demonstrated approaches [10,12,16–20], supercapacitors made by vertically aligned graphene electrodes, showed the most remarkable performance at high frequencies since this unique microstructure can minimize the electronic and ionic resistances and therefore increase the response rate of the device. Vertically aligned graphene electrodes have been successfully fabricated by various plasma-enhanced chemical vapor deposition techniques [21–24] or thermal decomposition of SiC [25]. However, the complexity, associated costs, and the elevated temperatures and vacuum system requirements make these methods challenging for device fabrication [12,18,25]. Recently, bipolar electrochemistry (BPE) has been developed as an alternative to the methods mentioned above. This technique is capable of in-situ integration of three steps of exfoliation, reduction, and deposition in an environmentally friendly, simple, and cost-effective fashion. Thus far, this technique has been successfully deployed to fabricate high-quality layered or vertically aligned 2D materials (graphene [26–31] and phosphorene [29,32,33]). To the best of our knowledge no studies have reported vertically aligned graphene on miniaturized interdigitated supercapacitors.

Typically, a BPE cell consists of a conductive material (bipolar electrode (BE)) placed wirelessly between two feeding electrodes of a conventional cell. When the conductivity of the BE is higher than that of the electrolyte, an interfacial potential difference (IPD) appears between the farthest edges of the BE. The magnitude of this IPD linearly depends on the distance between the farthest edges of the BE and the electric field in the solution. In the case that the IPD value is high enough, it can initiate redox reactions on the (anodic and cathodic) edges of BE [34,35] or electrochemical exfoliation of the BE if it is made of layered Van der Waals materials, such as graphite or black phosphorous [26–30,32,33]. The mechanism of this process has been studied in detail and reported in our previous work using a modified BPE design that allows to monitor either the anodic or cathodic reaction at a time [29]. We showed that both anions and cations from the electrolyte can intercalate into the BE lattice (i.e., graphite), which results in the simultaneous anodic and cathodic exfoliation of the BE. The exfoliated nanosheets are then dragged electrophoretically and deposited on the feeding electrodes surfaces thanks to the external field [29].

By considering the indisputable advantages of the BPE method over more conventional techniques for the synthesis of vertically aligned graphene and the necessities of addressing the frequency response of MSCs issues, this work investigates the compatibility of BPE for the development of high-performance on-chip MSC with a unique vertically aligned graphene microstructure. First, gold interdigitated microcurrent collectors (Au-MCC) were fabricated using the photolithography method. Next, BPE was used to in-situ exfoliate and deposit vertically aligned rGO on Au-MCC. The electrochemical performance of the fabricated MSCs in the time and frequency domains has been investigated, and the results showed outstanding capacitive storage capability at high frequencies (e.g., ~ 65.2 μF cm^{-2} at 120 Hz and 55 μF cm^{-2} at 1000 Hz). The MSC device has been tested and validated in a practical AC line filtering circuit in which the results are promising for on-chip microelectronic applications.

2. Materials and methods

2.1. Fabrication of Au-MCC

The fabrication of gold interdigitated MCC was conducted by photolithography. Fig. 1 (a) schematically depicts the fabrication process, which consists of the following steps: (1) A 4″ Si/SiN (100) wafer was first spin-coated by hexamethyldisilazane (HMDS) as the adhesion promoter and then by AZ 1518 (from Microchemicals) at a rotational speed of 500 rpm for 10 s, and then 2900 rpm for 30 s (2) Soft baking of the wafer was conducted for 60 s at 100 °C on a hot plate. (3) The wafer was then patterned by an OAI 800 mask aligner with a UV dose of 60 mJ cm^{-2} (4) After the exposure step, the photoresist development was carried out using diluted AZ 400 MIF (4:1 vol ratio of DI water to the developer) for ~60 s (5) The wafer was baked for 20 s at 65 °C and 70 s at 115 °C. (6) Next, O_2 plasma cleaning was conducted to remove the remaining photoresist by reactive ion etching (RIE) at 100 W power for 60 s (7) Then, e-beam evaporation was used for metallization of Cr/Au (20/100 nm) using a CHA evaporator. (8) Lift-off was carried out in sonication bath using AZ EBR solvent for 2 h, followed by acetone and isopropyl rinsing, and then N_2 drying. (9) To avoid the lateral growth and deposition of graphene in between the microelectrodes, a sacrificial photoresist layer was applied and patterned between the interdigitated electrodes by repeating steps 1 to 5 on the wafer with fabricated gold microelectrodes.

The optical microscopic checkout confirmed pattern transfer fidelity with interdigitated Au-MCC (thickness of ~120 nm) separated by sacrificial photoresist patterns (thickness of ~2 μm). There were 32

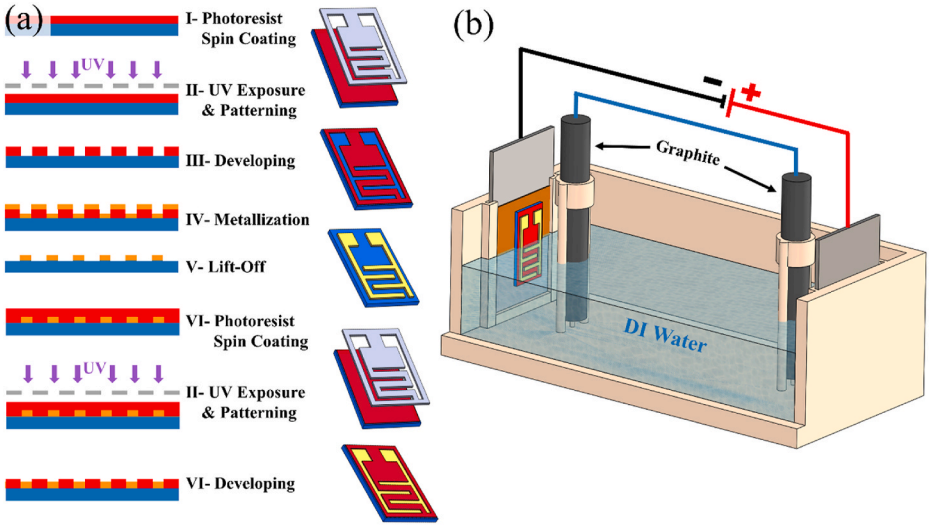

Fig. 1. (a) Illustration of the fabrication process of the interdigitated Au-MCC. (b) Schematic drawing of the BPE setup.

interdigital fingers in total on each Au-MCC (16 for each electrode side) with lengths and widths of 6040 μm and 100 μm, respectively. The design provided a geometrical surface area of 9.66 mm^2 on each side of Au-MCC. Based on the footprint area and the thickness of the electrodes, the device occupied as low as ~0.04 mm^3 without packaging. In addition to Au-MCC, carbon cloth and interdigitated carbon micro-electromechanical systems (C-MEMS) with 3D structure have also been used as the current collector to confirm the versatility of the BPE process for deposition of rGO on different substrates. The experimental details about the C-MEMS fabrication procedure have been reported in the previous studies [4–6,36].

2.2. Graphene synthesis and deposition

Fig. 1 (b) shows a schematic drawing of the modified BPE cell in DI water employed to deposit vertically aligned rGO on the Au-MCC, which was mounted on the negative feeding electrode (stainless steel 316, 2 × 1 cm^2) of the BPE cell. The distance between the two feeding electrodes is 9 cm. Two graphite rods were placed between the feeding electrodes in a way that the distance of the farthest edges of the two was 7 cm. These two graphite rods were electrically wired outside of the electrolyte. The BPE cell was designed and 3D printed (using PLA filament). A direct current (DC) voltage of 45 V was applied across the feeding electrodes for 24 h. In our previous study [29], it has been demonstrated that stirring the electrolyte of the BPE cell resulted in more uniform exfoliation-and-deposition of thin graphene sheets. Therefore, magnet stirring was added to the cell during the BPE process using a 1 cm magnet rod with a rotational speed of about 150 rpm. By the end of the BPE process, the MSCs were detached from the stainless steel feeding electrode and immersed in AZ EBR for 120 s to remove the sacrificial photoresist between the fingers. Finally, the substrates were thoroughly rinsed in isopropyl and DI water and then dried with N_2 gas.

2.3. Materials characterization

The morphology of the deposited graphene on the interdigitated Au-MCC was investigated using a JEOL 7000 scanning electron microscopy (SEM). Raman analysis was carried out on a Raman spectrometer (in backscattering configuration) equipped with an argon-ion laser (Spectra Physics Model 177, 514 nm, 400 mW) and HoloSpec f/l.8i, Kaiser optical spectrograph.

2.4. Electrochemical characterization of MSCs

The electrochemical performance of the MSCs has been evaluated in a two-electrode symmetric configuration, where one set of microelectrodes acted as the working electrode, and the other one was considered the counter electrode and reference electrode. The MSCs were immersed in 1 mol L^{-1} Na_2SO_4 for 1 h before starting the measurements. A VMP3 Bio-Logic multichannel potentiostat was used to evaluate the electrochemical performance of fabricated devices using cyclic voltammetry (CV), galvanostatic charge/discharge (GCD), and electrochemical impedance spectroscopy (EIS) techniques. The CV tests were conducted at scan rates from 2 to 5000 mV s^{-1}, and the GCD tests at loading currents from 25 to 250 μA cm^{-2}, both with the potential limits 0–0.8 V. For EIS measurements, the fully discharged MSCs (the DC voltage was around 0 V) were subjected to a 30 mV amplitude sinusoidal voltage with stepped frequencies from 1 MHz down to 100 mHz (6 frequency points per decade). The reported current and capacitance are normalized by the surface area of the microelectrodes (i.e., 9.66 mm^2).

2.5. AC line filtering circuit

To evaluate the performance of the developed MSC as an AC line filter, it was used in a standard AC to DC circuit in which an input 60 Hz, $V_{peak} = \pm 1.0$ V sinusoidal wave was rectified through a diode bridge resulting in a 120 Hz, $V_{peak} \simeq +0.8$ V rectified wave. Both open circuit and loaded circuit (with a 39 kΩ resistor) were used for validating the filter performance. The developed MSC was separated by a switch from the rest of the circuit, so that the change in the output waveform of the filter could be monitored when the MSC was connected to the circuit. Reference experiments were carried out using a commercial AEC (rated 10 μF, 16 V).

3. Results and discussion

Fig. 2 (a) shows a low-magnification SEM micrograph of the finger-like microelectrodes of the MSC device. Fig. 2 (b) presents a higher magnification SEM of the deposited graphene. The figure shows the formation of high surface area and porous structure of vertically aligned graphene nanosheets. It can be seen that graphene sheets (with dimensions in the order of several hundred nanometers) formed a porous network on the current collector (similar to the structure reported in the previous study [27]). Such geometrical features are expected to be advantageous for the high-frequency response and power performance of MSC devices by facilitating the rapid diffusion of ionic species [17,20]. Fig. 2 (c) presents the Raman spectrum of the deposited graphene on the Au-MCC substrates depicting typical Raman peaks of graphene materials (i.e., D-band at ~1350 cm^{-1}, G-band at ~1609 cm^{-1}, 2D peak at ~2700 cm^{-1}, and D + G peak ~2910 cm^{-1} [37]). It can be seen that the intensity of the D-band is lower than the one of the G-band, which confirms the formation of highly reduced graphene oxide (rGO) on the surface (I_D to I_G intensity ratio is about 0.78) [27,37–39]. Similar results have been reported in our previous study for graphene deposited on the negative stainless steel feeding electrode of the BPE setup [27]. In addition to the gold microelectrode substrate, carbon cloth (Fig. S1 (a) and (b)) and C-MEMS microelectrodes (Fig. S1 (c) and (d)) have also been tried as current collectors in the BPE process. The successful deposition of vertically aligned graphene nanosheets on all of these substrates indicates the compatibility and versatility of the BPE process for deposition of rGO on various types of conductive substrates. Furthermore, the comparison of Figs. S2 and S3 clearly demonstrate the effectiveness of high-fidelity pattern formation using the sacrificial photoresist layer. Without the sacrificial layer (Fig. S2), the residue graphene can be observed between the fingers; while with the application of sacrificial layer (Fig. S3), deposition of graphene can be observed only on top of the conductive parts of the substrate after dissolving the photoresist.

In this study, the CV, GCD, and EIS measurement techniques were conducted to study the time domain and frequency domain performance of rGO-MSC, and as-is Au-MCC substrate for comparison. Fig. 3 (a) and S4 (a) present the CVs results of rGO-MSC and Au-MCC, respectively. The shapes of the curves are almost rectangular without any detectable current peaks over the covered voltage window from 0 to 0.8 V. This indicates that no faradaic reactions were taking place on the electrodes of these devices and that the charge storage mechanism is predominantly physical through the formation of double-layer structure (as expected for carbon-based electrodes). An increased tilting of the CV profiles with respect to the x-axis at higher charging/discharging rates was also remarked, which indicates increased resistive behavior in the device at the expense of capacitive energy storage.

The GCD results of rGO-MSC and Au-MCC at different current densities are shown in Fig. 3 (b) and S4 (b), respectively. The GCD curves show relatively symmetric and quasi-triangular shapes at all tested current densities indicating close-to-ideal capacitive behavior of both rGO-MSC and Au-MCC. In the GCD test, the sudden voltage drop at the beginning of the discharge curve is typically associated with the irreversible ohmic losses (i.e., iR_s drop) in the series resistance of the MSCs. The GCD curves obtained in this study do not show a substantial voltage drop for any of the current densities we applied, indicating relatively low internal resistance of the MSCs. A comparison between the discharge time of the Au-MCC and rGO-MSC devices reveals that the

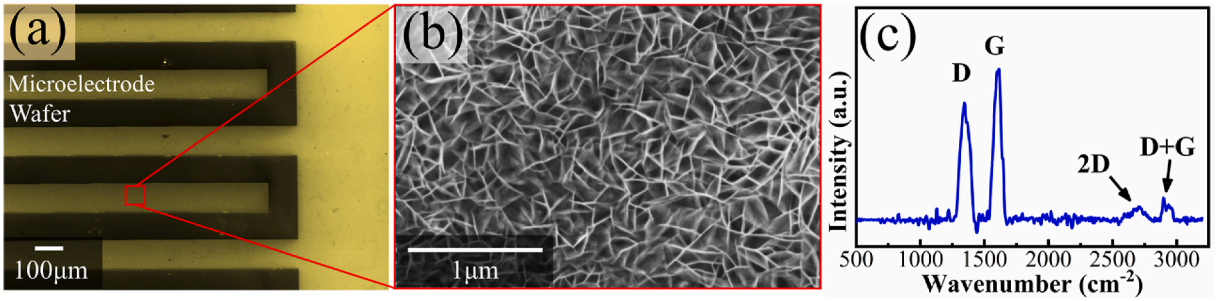

Fig. 2. (a) Low magnification SEM image of microelectrodes. (b) SEM image of the vertically aligned graphene nanosheets deposited on the microelectrodes. (c) A Raman spectrum of deposited graphene.

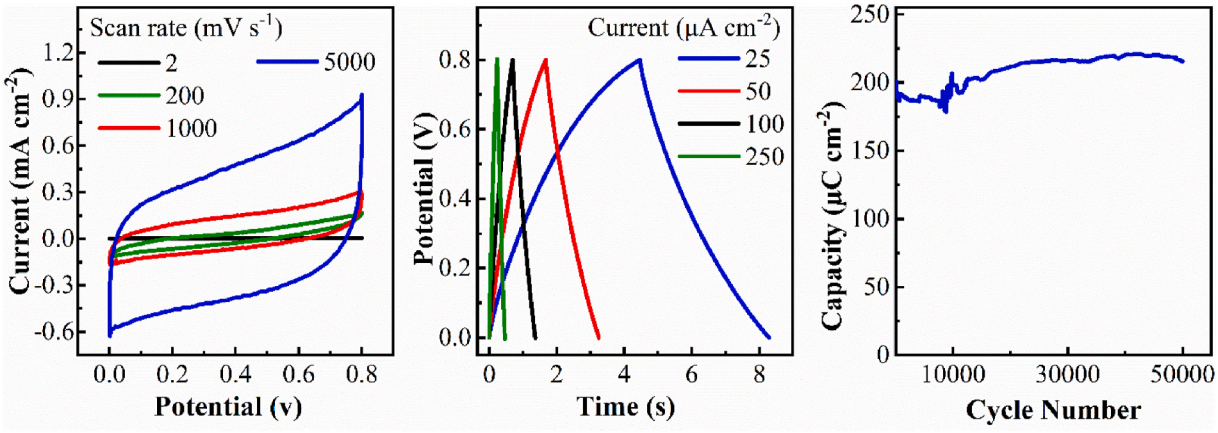

Fig. 3. (a) Cyclic voltammetry at scan rates of 2, 200, 1000 and 5000 mV s^{-1}, (b) galvanostatic charge-discharge results at current densities of 25, 50, 100 and 250 μA cm^{-2}, and (c) the cycling performance (charge-discharge at 25 μA cm^{-2}) of the fabricated rGO-MSC.

deposition of rGO by the BPE technique can significantly increase the capacity of the MSCs for storing the charge. It is evident that discharge time increased by about 30 times (from 0.126 s to 3.829 s) at the discharge current of 25 μA cm^{-2}.

The non-ideal capacitive features in the current-voltage and voltage-time profiles are well-known for electrochemical capacitive devices, i.e., nonlinear charge-voltage profiles and thus non-constant, voltage, and rate-dependent characteristics capacitance function [40–42]. In response to an applied voltage, a net charge is accumulated on the surface of an electrode, which brings electrolytic counterions from the immediate vicinity of the electrode surface to rearrange themselves accordingly to balance this charge. The layer of charge in the electrolyte is then balanced by the formation of a second layer of concentration-dependent, diffuse charge. Subsequently, the ions in the double-layer structure rearrange and generate a current when the electrode voltage is changed —depending on its rate— as is the case of CV tests. Therefore, from the current-voltage dynamics (CV) and voltage-time profiles (GCD), it is difficult to estimate a characteristic capacitive function as commonly done in the literature from the simple division of charge by voltage. Nonetheless, for the sake of comparison, we computed the ratio $\overline{C} = 2\int i(V)dV/(v\Delta VA)$ (in units of $C.V^{-1}cm^{-2}$) using data from the CV curves, where $\overline{C}$ can be viewed as averaged value relating the voltage-averaged current (expressed by $\bar{I} = \Delta V^{-1}\int i(V)dV$) to the voltage scan rate v, and normalized with respect to the micro-electrode's geometric area A on each side of the MSCs. The computed values of $\overline{C}$ at the different scan rates of 2, 10, 50, 100, 200, 1000 and 5000 mV s^{-1} were found to be 640, 454, 346, 315, 281, 194, and 161 $C.V^{-1}cm^{-2}$ (equivalent to μF cm^{-2}) respectively for rGO-MSC, and 61, 27, 12, 9, 8, 7 and 5 $C.V^{-1}cm^{-2}$ (equivalent to μF cm^{-2}) respectively for Au-MCC device. Applying the cyclic triangular excitation in CV with the voltage scan rates of 2, 10, 50, 100, 200, 1000, and 5000 mV s^{-1} is similar to exciting the device at the fundamental frequencies of 1.25 mHz, 6.25 mHz, 31.25 mHz, 62.5 mHz, 125 mHz, 625 mHz, and 3.125 Hz respectively, which explains the decrease in values of $\overline{C}$ as the scan rate is increased, as will be discussed further in the EIS results below.

In order to investigate the capacity retention and cyclic performance of the fabricated devices, a rGO-MSC was charged and discharged 50,000 consecutive times at the current density of 25 μA cm^{-2}. Fig. 3 (c) shows a plot of discharge capacity vs. cycle number. The 12% relative increase of capacity from the first to the last cycle without fading indicates an excellent stability performance of the device. Such behavior has been reported in other research studies [5] and can be explained by the electrochemical activation of the carbon materials during the charge-discharge process and/or an increased wettability of the electrodes.

EIS analysis was conducted to study the performance of the MSCs as a function of frequency. The Nyquist plots, which are the illustration of the imaginary (-Im(Z)) vs. real (Re(Z)) parts of the impedance, are presented in Fig. 4 (a). The impedance of an ideal capacitor is purely imaginary and does not have a real part (i.e., $Z = -j/(\omega C)$ with C being the capacitance and ω the angular frequency), i.e., vertical line parallel to the y-axis. Both Au-MCC and rGO-MSC (fresh or after 50000 of charge/discharge cycles) showed some small deviations from the ideal capacitive behavior without any sizable, diffusion-related Warburg region. Therefore, we used an equivalent circuit model of a series resistance R_s with a constant phase element (CPE) of total impedance being [27,43,44].

$$Z = R_s + \frac{1}{(j\omega)^{\alpha}C_{\alpha}} \quad (1)$$

to fit the data from 100 mHz to about 50 kHz. In this model, the value of

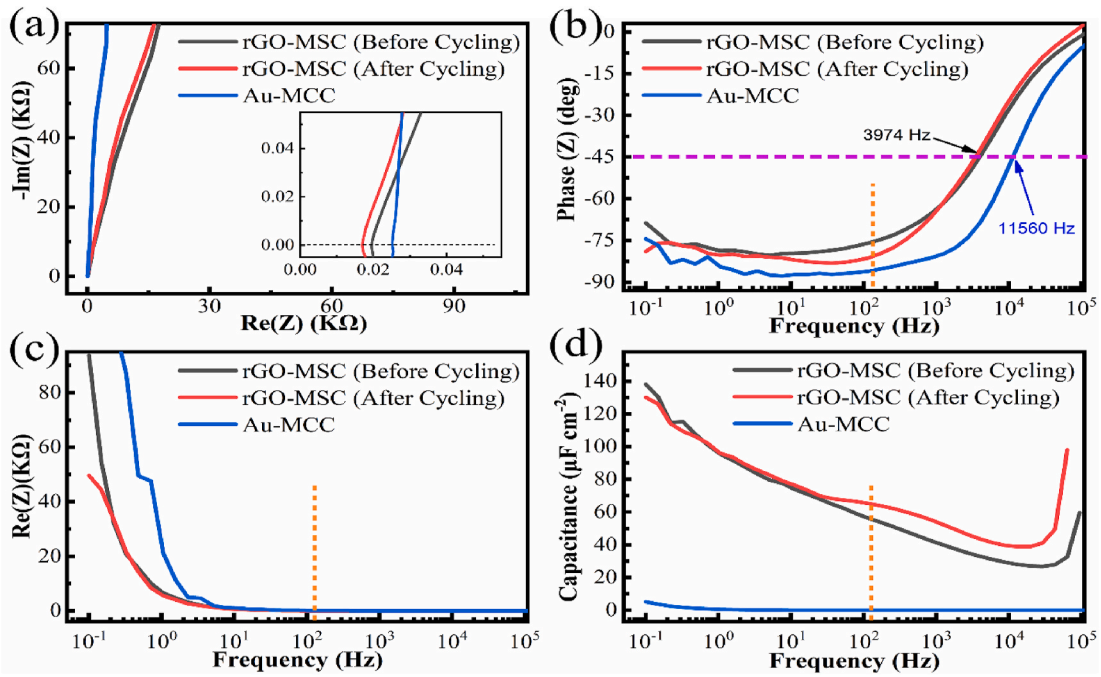

Fig. 4. (a) Complex-plane representation of real vs. imaginary part of impedance (Nyquist plot), (b) impedance phase angle as a function of frequency (bode phase plot), (c) the device resistance as a function of frequency, and (d) specific areal capacitance as a function of frequency, for Au-MCC and rGO-MSC before and after cycling.

α is between 1 and 0, C_α is a positive constant in units of F s^{a-1}, and $j^\alpha = \cos\left(\frac{\alpha\pi}{2}\right) + j\sin\left(\frac{\alpha\pi}{2}\right)$ (Euler formula) [27,43,44]. At the limiting values of 1 and 0 for α, the impedance function simplifies to that of an ideal capacitor and a resistor, respectively. Using equation (1), and by manually setting the values of R_s taken from the high-frequency intercepts of the impedance data with the real axis, we found an impedance phase angle $-\frac{\alpha\pi}{2} = -83$ deg for Au-MCC device, whereas the phase angle for rGO-MSC is −73 deg before cycling and −78 deg after cycling.

The deviation from ideal behavior can also be seen from the Bode phase plots in Fig. 4 (b), knowing that the phase angle for an ideal capacitor is −90 deg, independently of the frequency and voltage. As it can be seen, all of the devices showed some deviations from the ideal capacitive behavior with relatively constant phase angle in the low-frequency region (lower than ~1000 Hz for rGO-MSCs and lower than ~5000 Hz for Au-MCC). The minimum phase angle for rGO-MSC after cycling and Au-MCC were −83.2 deg and −87.7 deg, respectively. Moreover, as the frequency increased, the phase angles tended quickly towards the resistive behavior of zero impedance phase angle. When the phase angle is between −90 deg and −45 deg, the imaginary part of the impedance is larger than the real part. The frequency at which the imaginary and real parts become equal (i.e., the phase angle is −45 deg) is called cut-off frequency or characteristic frequency (f_0) that is commonly used as a figure of comparison between devices (Table 1). This parameter reveals up to what frequency range the device can be more effectively used as capacitive energy storage, albeit with some resistive losses that depend on the extent of the dispersion coefficient α. The inverse of the cut-off frequency is referred to the relaxation time constant ($\tau_0 = 1/f_0$), which is the minimum time needed to discharge all the energy from the device with an efficiency greater than 50% [4,45]. From Fig. 4 (b), the cut-off frequency for Au-MCC was found to be as high as 11560 Hz. For rGO-MSC, a frequency of 3974 Hz for the freshly prepared device was found, whereas, after 50000 consecutive charge/-discharge cycles with 25 μA cm^{-2}, that value dropped to just 3486 Hz, showing the excellent (mechanical and chemical) stability of the rGO material, the adopted MSC design, and fabrication technique. The corresponding relaxation time constants are 8.6 μs for Au-MCC, and 251 μs and 286 μs for the rGO-MSC before and after cycling, respectively. Compared to other microcapacitors [46–51], our results indicate that BPE-based vertically aligned rGO can deliver one of the shortest time constants.

Table 1
The performance of different micro-supercapacitors fabricated to operate in AC line filtering application.

Materials	φ_{120}(°)	f_0(Hz)	C_A(μF cm^{-2})	Ref
Azulene-bridged coordination polymer framework (PiCBA)	−73	3620	0.014[a,b] (at 120 Hz)	[52]
Direct laser writing of graphene made from chemical vapor deposition	−76.2	2025	15[a] (at 200 V s^{-1})	[46]
Charge transfer salt and graphene heterostructure-based	−73.2	3056	151 (at 120 Hz)	[47]
Metallic 1T-Phase MoS_2	−79[a]	1221	NA	[48]
RIE reduced graphene oxide	−68[a]	3579	13.5 (at 200 V s^{-1})	[49]
Composite of MXene and MWCNT	−79[a]	2000[a]	600[a] (at 120 Hz)	[50]
Inkjet-Printed NiO	−25[a]	33	NA	[51]
Catechol-coordinated framework film (Cu-DTHAB film)	−84	16374	0.96[a,b] (at 120 Hz)	[53]
High aspect ratio 3D nanoporous gold	−61	250[a]	800[a] (at 200 V s^{-1})	[54]
Oriented coordination polymer (Cobalt benzenetetramine tetrahydrochloride)	−78.6	6812	9[a,b] (at 120 Hz)	[55]
Reduced Graphene Oxide and Carbon Nanotube Composites	−62	208	NA	[10]
B/N-Enriched semi-conductive polymer film	−67	1910	28[a,b] (at 200 V s^{-1})	[56]
Present work	**−81.2**	**3486**	**65.2 (at 120 Hz)**	

[a] Extracted from a graph of the original article, which may have caused some minor errors in the data readout.
[b] The data is converted from volumetric specific capacitance to the specific areal capacitance.

The real part of the impedance as a function of frequency for the

tested devices is plotted in Fig. 4 (c). All devices show very low resistance (0.03 kΩ) at frequencies higher than 1 Hz. Specifically, at 120 Hz, the devices show mostly capacitive behavior with negligible resistive behavior. The capacitance of MSCs at different frequencies can be computed from $\mathrm{Im}(Z) = -j/(\omega C)$, where $\omega = 2\pi f$, which has been further normalized with respect to the geometrical area of the current collector at each side. The plot is provided in Fig. 4 (d). At the frequencies of 0.1 Hz, 1 Hz, and 1250 Hz, the corresponding capacitance for rGO-MSC after 50000 of GCD cycles was found to be 130 μF cm^{-2}, 96 μF cm^{-2}, and 52 μF cm^{-2} respectively, whereas for Au-MCC it was 5.29 μF cm^{-2}, 0.59 μF cm^{-2} and 0.0011 μF cm^{-2}, respectively. These results are consistent with those of CV and GCD tests. Table 1 provides a performance summary of recent MSC devices designed to operate at high frequencies and AC filtering applications. The data is summarized based on the characteristic frequency (f_0), the phase angle at 120 Hz (φ_{120}), and specific areal capacitance. It worth noting that the specific areal capacitances were computed at 120 Hz either using frequency domain analysis or at 200 V s^{-1} (i.e., the fundamental frequency of 100 Hz for a voltage window of 1 V). The performance summary suggests that the rGO-MSC fabricated in this study provides one of the best-performing devices. It is worth noting that, as reported recently in Refs. [40–42], the frequency-domain definition of capacitance being the division of frequency-domain charge by voltage is better recommended for characterizing non-ideal capacitive devices as it is in line with the definition of impedance. Furthermore, if one assumes such a definition, we believe the appropriate way for computing the corresponding time-domain capacitance function is by deconvolution (convolution theorem of the Fourier transform) and not the division of charge by voltage as done for the computation of $\overline{C}$.

Finally, in order to evaluate the practical application of the fabricated rGO-MSC at high frequencies, it has been tested in an AC - DC filtering circuit (Fig. 5 (a), see section 2.5 for more details). The voltage output when the rGO-MSC device was not connected to any load (R = ∞) is illustrated in Fig. 5 (b). As evident, the pulsing 120 Hz, $V_{peak} \simeq +0.8$ V rectified signal was perfectly flattened when the rGO-MSC was connected to the circuit (switch on). However, it is worth noting that for valid performance evaluations, it is essential to connect a parallel load to the capacitive device to evaluate its performance in AC filtering applications. The flattening can be done at open circuit conditions with any device, including a parasitic capacitance at the target frequency. In contrast, when a load is connected to the circuit, it will drain the stored energy from the capacitor when the input voltage is lower than that across the capacitor. In this situation, the magnitude of the fluctuations (ripple) in the flattened signal will change as a function of the stored capacity at that specific frequency. In light of the performance mechanism mentioned above, the performance of the rGO-MSC device as a filtering capacitor was evaluated when a resistor (R = 1 kΩ, 39 kΩ, and 100 kΩ) was added to the circuit as a working load. The typical filtering performance with a 39 kΩ resistor is plotted in Fig. 5 (c), confirming that the rGO-MSC could successfully filter the pulsing signal even when a resistor simultaneously discharged it. The same experiment has been conducted using a 10 μF AEC, and the results are shown in Fig. 5 (d). Although the nominal capacitance of the AEC was almost three times higher than that of the rGO-MSC device (10 μF vs. 3.13 μF at 120 Hz), their filtering outputs are similar. However, the AEC (with a volume of about 215 mm^3) is much bulkier than the miniaturized on-chip MSC.

The high-frequency response of rGO-MSC can be attributed to the miniaturized MSCs design, and thus shorter length for ionic diffusion in response to external excitations. In addition to the highly structured and stable vertically aligned rGO electrodes (obtained by BPE) provides further enhancements in the charge storage capabilities. It is important be noted that BPE has excellent compatibility with semiconductor processing and could be applied to not only graphene but also for deposition of other 2D layered materials for forming morphogenic materials and interfaces with controllable morphologies, orientation, and structures. In principle, the ease of fabrication of microstructured electrodes and devices by the versatile, cost-efficient, and environmentally-friendly BPE process can be applied for fabricating other micro-sized electronic devices such as batteries, sensors, electrochemical transistors, and memristors, to cite a few.

4. Conclusion

In summary, we demonstrated a new strategy and approach for preparing vertically aligned graphene-based MSCs for high-frequency applications. A modified BPE process was employed to deposit vertically aligned and highly reduced rGO nanosheets on an Au-MCC current collector. The occurrence of lateral growth of graphene sheets between

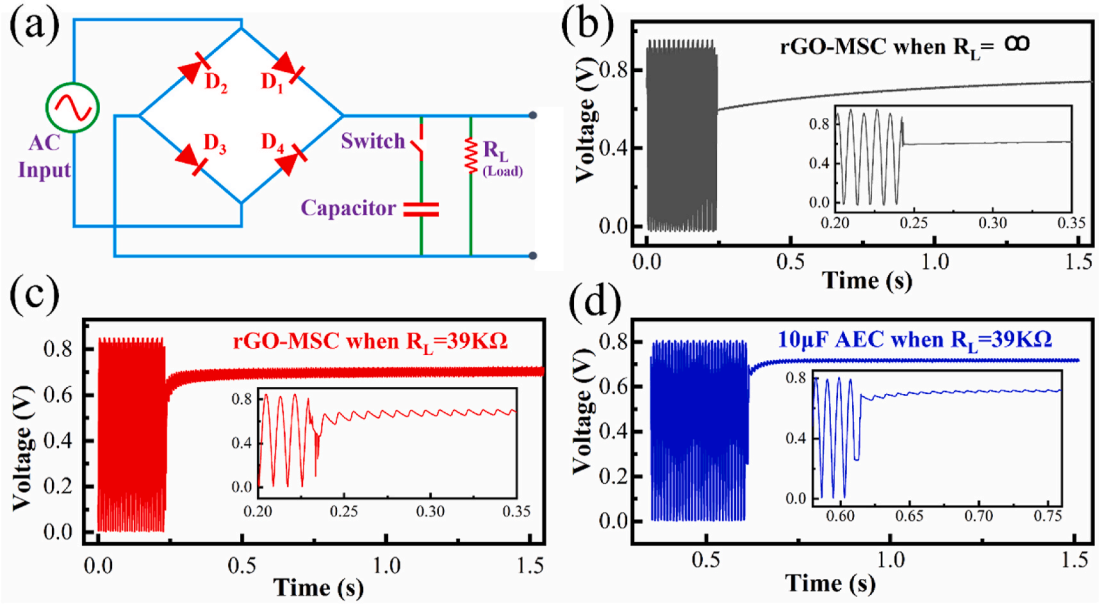

Fig. 5. (a) Schematic of the circuit which is used as the AC to DC convertor. The smoothing capability of the rGO-MSC subjected to a rectified 120 Hz wave (b) when no load was connected to the circuit, (c) when a 39 KΩ resistor was connected to the circuit as a load, (d) when MSC was replaced by a 10 μF commercial AEC for comparison.

the gold fingers during the BPE process has been prevented by adding a sacrificial layer of photoresist between the fingers. The time-domain and frequency-domain electrochemical analysis of the rGO-MSC devices demonstrated excellent stability and high performance for both energy storage at close-to-dc- frequencies as well as filtering capabilities for AC line filtering applications. In particular, from the EIS results, this study demonstrated that not only the deviation from ideal capacitive behavior was very small at low frequencies, but also promising capacitive performance at the high frequencies was observed. The use of rGO-MSCs in a standard 60 Hz AC filtering circuit showed that the device accomplished excellent flattening performance comparable to a relatively bulky and massive off-the-shelf AEC.

CRediT authorship contribution statement

Iman Khakpour: designed the experiments, carried out all experiments and processed the data presented here,: discussed and interpreted results and commented on the manuscript, Writing – original draft. **Amin Rabiei Baboukani:** carried out all experiments and processed the data presented here, discussed and interpreted results and commented on the manuscript. **Shahrzad Forouzanfar:** carried out all experiments and processed the data presented here, discussed and interpreted results and commented on the manuscript. **Anis Allagui:** discussed and interpreted results and commented on the manuscript, Writing – original draft. **Chunlei Wang:** discussed and interpreted results and commented on the manuscript, Writing – original draft, All authors participated in the preparation and review of the manuscript.

Declaration of competing interest

The authors declare that they have no known competing financial interests or personal relationships that could have appeared to influence the work reported in this paper.

Acknowledgments

This work was partially supported by the US National Science Foundation awards 1611088 and 1506640. The authors acknowledge Precise Advanced Technologies and Health Systems for Underserved Populations (PATHS-UP) Engineering Research Center (ERC). Iman Khakpour acknowledges Doctoral Evidence Acquisition (DEA) Fellowship and Dissertation Year Fellowship (DYF) from Florida International University. The authors would like to thank the staff members of the Centers Study of Matter at Extreme Conditions (CeSMEC) and Advanced Materials Engineering Research Institute (AMERI) at FIU.

Appendix A. Supplementary data

Supplementary data to this article can be found online at https://doi.org/10.1016/j.jpowsour.2021.230701.

References

[1] R. Agrawal, C. Wang, On-chip asymmetric microsupercapacitors combining reduced graphene oxide and manganese oxide for high energy-power tradeoff, Micromachines 9 (8) (2018) 399.
[2] F. Bu, W. Zhou, Y. Xu, Y. Du, C. Guan, W. Huang, Recent developments of advanced micro-supercapacitors: design, fabrication and applications, npj Flexible Electronics 4 (1) (2020) 1–16.
[3] J. Zhang, G. Zhang, T. Zhou, S. Sun, Recent developments of planar micro-supercapacitors: fabrication, properties, and applications, Adv. Funct. Mater. 30 (19) (2020) 1910000.
[4] M. Beidaghi, C. Wang, Micro-supercapacitors based on three dimensional interdigital polypyrrole/C-MEMS electrodes, Electrochim. Acta 56 (25) (2011) 9508–9514.
[5] M. Beidaghi, W. Chen, C. Wang, Electrochemically activated carbon micro-electrode arrays for electrochemical micro-capacitors, J. Power Sources 196 (4) (2011) 2403–2409.
[6] E. Adelowo, A.R. Baboukani, O. Okpowe, I. Khakpour, M. Safa, C. Chen, C. Wang, A high-energy aqueous on-chip lithium-ion capacitor based on interdigital 3D carbon microelectrode arrays, J. Power Sources 455 (2020) 227987.
[7] P. Huang, C. Lethien, S. Pinaud, K. Brousse, R. Laloo, V. Turq, M. Respaud, A. Demortiere, B. Daffos, P.-L. Taberna, On-chip and freestanding elastic carbon films for micro-supercapacitors, Science 351 (6274) (2016) 691–695.
[8] D. Pech, M. Brunet, P.-L. Taberna, P. Simon, N. Fabre, F. Mesnilgrente, V. Conédéra, H. Durou, Elaboration of a microstructured inkjet-printed carbon electrochemical capacitor, J. Power Sources 195 (4) (2010) 1266–1269.
[9] B. Dousti, Y.I. Choi, S.F. Cogan, G.S. Lee, A high energy density 2D microsupercapacitor based on an interconnected network of a horizontally aligned carbon nanotube sheet, ACS Appl. Mater. Interfaces 12 (44) (2020) 50011–50023.
[10] M. Beidaghi, C. Wang, Micro-supercapacitors based on interdigital electrodes of reduced graphene oxide and carbon nanotube composites with ultrahigh power handling performance, Adv. Funct. Mater. 22 (21) (2012) 4501–4510.
[11] M. Beidaghi, Y. Gogotsi, Capacitive energy storage in micro-scale devices: recent advances in design and fabrication of micro-supercapacitors, Energy Environ. Sci. 7 (3) (2014) 867–884.
[12] J.R. Miller, Engineering electrochemical capacitor applications, J. Power Sources 326 (2016) 726–735.
[13] J. Libich, J. Máca, J. Vondrák, O. Čech, M. Sedlaříková, Supercapacitors: properties and applications, Journal of Energy Storage 17 (2018) 224–227.
[14] B. Lu, X. Jin, Q. Han, L. Qu, Planar graphene-based microsupercapacitors, Small (2021) 2006827.
[15] M. Beidaghi, Z. Wang, L. Gu, C. Wang, Electrostatic spray deposition of graphene nanoplatelets for high-power thin-film supercapacitor electrodes, J. Solid State Electrochem. 16 (10) (2012) 3341–3348.
[16] N. Islam, M.N.F. Hoque, W. Li, S. Wang, J. Warzywoda, Z. Fan, Vertically edge-oriented graphene on plasma pyrolyzed cellulose fibers and demonstration of kilohertz high-frequency filtering electrical double layer capacitors, Carbon 141 (2019) 523–530.
[17] Z. Fan, N. Islam, S.B. Bayne, Towards kilohertz electrochemical capacitors for filtering and pulse energy harvesting, Nano Energy 39 (2017) 306–320.
[18] J.R. Miller, R. Outlaw, B. Holloway, Graphene double-layer capacitor with ac line-filtering performance, Science 329 (5999) (2010) 1637–1639.
[19] M. Cai, R.A. Outlaw, R.A. Quinlan, D. Premathilake, S.M. Butler, J.R. Miller, Fast response, vertically oriented graphene nanosheet electric double layer capacitors synthesized from C2H2, ACS Nano 8 (6) (2014) 5873–5882.
[20] J.R. Miller, Perspective on electrochemical capacitor energy storage, Appl. Surf. Sci. 460 (2018) 3–7.
[21] M. Zhu, R. Outlaw, M. Bagge-Hansen, H. Chen, D. Manos, Enhanced field emission of vertically oriented carbon nanosheets synthesized by C2H2/H2 plasma enhanced CVD, Carbon 49 (7) (2011) 2526–2531.
[22] D. Premathilake, R.A. Outlaw, S.G. Parler, S.M. Butler, J.R. Miller, Electric double layer capacitors for ac filtering made from vertically oriented graphene nanosheets on aluminum, Carbon 111 (2017) 231–237.
[23] R. Thomas, G.M. Rao, Synthesis of 3-dimensional porous graphene nanosheets using electron cyclotron resonance plasma enhanced chemical vapour deposition, RSC Adv. 5 (103) (2015) 84927–84935.
[24] A. Malesevic, R. Vitchev, K. Schouteden, A. Volodin, L. Zhang, G. Van Tendeloo, A. Vanhulsel, C. Van Haesendonck, Synthesis of few-layer graphene via microwave plasma-enhanced chemical vapour deposition, Nanotechnology 19 (30) (2008) 305604.
[25] S. Zheng, Z. Li, Z.-S. Wu, Y. Dong, F. Zhou, S. Wang, Q. Fu, C. Sun, L. Guo, X. Bao, High packing density unidirectional arrays of vertically aligned graphene with enhanced areal capacitance for high-power micro-supercapacitors, ACS Nano 11 (4) (2017) 4009–4016.
[26] A. Allagui, M.A. Abdelkareem, H. Alawadhi, A.S. Elwakil, Reduced graphene oxide thin film on conductive substrates by bipolar electrochemistry, Sci. Rep. 6 (2016) 21282.
[27] I. Khakpour, A. Rabiei Baboukani, A. Allagui, C. Wang, Bipolar exfoliation and in situ deposition of high-quality graphene for supercapacitor application, ACS Appl. Energy Mater. 2 (7) (2019) 4813–4820.
[28] A. Allagui, J.M. Ashraf, M. Khalil, M.A. Abdelkareem, A.S. Elwakil, H. Alawadhi, All-solid-state double-layer capacitors using binderless reduced graphene oxide thin films prepared by bipolar electrochemistry, ChemElectroChem 4 (8) (2017) 2084–2090.
[29] I. Khakpour, A.R. Baboukani, A. Allagui, A.A. Hachicha, C. Wang, On the mechanistic pathways of exfoliation-and-deposition of graphene by bipolar electrochemistry, Nanotechnology 32 (34) (2021) 345603.
[30] H. Hashimoto, Y. Muramatsu, Y. Nishina, H. Asoh, Bipolar anodic electrochemical exfoliation of graphite powders, Electrochem. Commun. 104 (2019) 106475.
[31] S. Forouzanfar, I. Khakpour, F. Alam, N. Pala, C. Wang, Novel application of electrochemical bipolar exfoliated graphene for highly sensitive disposable label-free cancer biomarker aptasensors, Nanoscale Adv. 3 (2021) 5948–5958, https://doi.org/10.1039/D1NA00470K.
[32] A.R. Baboukani, I. Khakpour, V. Drozd, A. Allagui, C. Wang, Single-step exfoliation of black phosphorus and deposition of phosphorene via bipolar electrochemistry for capacitive energy storage application, J. Mater. Chem. 7 (44) (2019) 25548–25556.
[33] A.R. Baboukani, I. Khakpour, C. Wang, Bipolar Exfoliation of Black Phosphorous into Phosphorene, Google Patents, 2020.
[34] G. Loget, D. Zigah, L. Bouffier, N. Sojic, A. Kuhn, Bipolar electrochemistry: from materials science to motion and beyond, Accounts Chem. Res. 46 (11) (2013) 2513–2523.

[35] C.A. Sequeira, D.S. Cardoso, M.L.F. Gameiro, Bipolar electrochemistry, a focal point of future research, Chem. Eng. Commun. 203 (8) (2016) 1001–1008.
[36] S. Forouzanfar, N. Pala, M. Madou, C. Wang, Perspectives on C-MEMS and C-NEMS biotech applications, Biosens. Bioelectron. (2021) 113119.
[37] A. Kaniyoor, S. Ramaprabhu, A Raman spectroscopic investigation of graphite oxide derived graphene, AIP Adv. 2 (3) (2012), 032183.
[38] N. Parveen, M.O. Ansari, M.H. Cho, Correction: simple route for gram synthesis of less defective few layered graphene and its electrochemical performance, RSC Adv. 6 (21) (2016) 17384–17385.
[39] A.C. Ferrari, D.M. Basko, Raman spectroscopy as a versatile tool for studying the properties of graphene, Nat. Nanotechnol. 8 (4) (2013) 235–246.
[40] A. Allagui, A.S. Elwakil, C. Psychalinos, Decoupling the magnitude and phase in a constant phase element, J. Electroanal. Chem. 888 (2021) 115153.
[41] A. Allagui, A.S. Elwakil, M.E. Fouda, Revisiting the time-domain and frequency-domain definitions of capacitance, IEEE Trans. Electron. Dev. 68 (6) (2021) 2912–2916.
[42] A. Allagui, A.S. Elwakil, H. Eleuch, Highlighting a Common Confusion in the Computation of Capacitance of Electrochemical Energy Storage Devices, ACS Publications, 2021, pp. 9591–9592.
[43] A. Allagui, T.J. Freeborn, A.S. Elwakil, M.E. Fouda, B.J. Maundy, A.G. Radwan, Z. Said, M.A. Abdelkareem, Review of fractional-order electrical characterization of supercapacitors, J. Power Sources 400 (2018) 457–467.
[44] A. Allagui, T.J. Freeborn, A.S. Elwakil, B.J. Maundy, Reevaluation of performance of electric double-layer capacitors from constant-current charge/discharge and cyclic voltammetry, Sci. Rep. 6 (2016) 38568.
[45] P. Taberna, P. Simon, J.-F. Fauvarque, Electrochemical characteristics and impedance spectroscopy studies of carbon-carbon supercapacitors, J. Electrochem. Soc. 150 (3) (2003) A292.
[46] J. Ye, H. Tan, S. Wu, K. Ni, F. Pan, J. Liu, Z. Tao, Y. Qu, H. Ji, P. Simon, Direct laser writing of graphene made from chemical vapor deposition for flexible, integratable micro-supercapacitors with ultrahigh power output, Adv. Mater. 30 (27) (2018) 1801384.
[47] D. Zhao, W. Chang, C. Lu, C. Yang, K. Jiang, X. Chang, H. Lin, F. Zhang, S. Han, Z. Hou, Charge transfer salt and graphene heterostructure-based micro-supercapacitors with alternating current line-filtering performance, Small 15 (48) (2019) 1901494.
[48] C. Xu, L. Jiang, X. Li, C. Li, C. Shao, P. Zuo, M. Liang, L. Qu, T. Cui, Miniaturized high-performance metallic 1T-Phase MoS2 micro-supercapacitors fabricated by temporally shaped femtosecond pulses, Nano Energy 67 (2020) 104260.
[49] Z.S. Wu, K. Parvez, X. Feng, K. Müllen, Graphene-based in-plane micro-supercapacitors with high power and energy densities, Nat. Commun. 4 (1) (2013) 1–8.
[50] S. Xu, W. Liu, B. Hu, X. Wang, Circuit-integratable high-frequency micro supercapacitors with filter/oscillator demonstrations, Nano Energy 58 (2019) 803–810.
[51] P. Giannakou, M.G. Masteghin, R.C. Slade, S.J. Hinder, M. Shkunov, Energy storage on demand: ultra-high-rate and high-energy-density inkjet-printed NiO micro-supercapacitors, J. Mater. Chem. 7 (37) (2019) 21496–21506.
[52] C. Yang, K.S. Schellhammer, F. Ortmann, S. Sun, R. Dong, M. Karakus, Z. Mics, M. Löffler, F. Zhang, X. Zhuang, Coordination polymer framework based on-chip micro-supercapacitors with AC line-filtering performance, Angew. Chem. Int. Ed. 56 (14) (2017) 3920–3924.
[53] T. Yu, Y. Wang, K. Jiang, G. Zhai, C. Ke, J. Zhang, J. Li, D. Tranca, E. Kymakis, X. Zhuang, Catechol-coordinated framework film-based micro-supercapacitors with AC line filtering performance, Chem. –A Eur. J. (2021) 6340–6347.
[54] F. Xia, S. Xu, B. Hu, X. Jia, X. Wang, High-frequency micro supercapacitors based on high-aspect-ratio 3D nanoporous gold interdigital electrodes for on-chip filtering, in: 2019 20th International Conference on Solid-State Sensors, Actuators and Microsystems & Eurosensors XXXIII (TRANSDUCERS & EUROSENSORS XXXIII), IEEE, 2019, pp. 1447–1450.
[55] W. Hua, J. Xiu, F. Xiu, Z. Zhang, J. Liu, L. Lai, W. Huang, Micro-supercapacitors based on oriented coordination polymer thin films for AC line-filtering, RSC Adv. 8 (53) (2018) 30624–30628.
[56] Z. Chen, Y. Chen, Y. Zhao, F. Qiu, K. Jiang, S. Huang, C. Ke, J. Zhu, D. Tranca, X. Zhuang, B/N-enriched semi-conductive polymer film for micro-supercapacitors with AC line-filtering performance, Langmuir 37 (7) (2021) 2523–2531.